


Article

A Simple and Compact Laser Scattering Setup for Characterization of a Pulsed Low-Current Discharge

Michał Szulc ^{1,*} , Günter Forster ¹, Jose-Luis Marques-Lopez ² and Jochen Schein ¹

¹ Institute for Plasma Technology and Mathematics, Faculty of Electrical Engineering and Information Technology, Universität der Bundeswehr München, Werner-Heisenberg-Weg 39, 85577 Neubiberg, Germany; guenter.forster@unibw.de (G.F.); js@unibw.de (J.S.)

² Institute for Measurement and Automation Technology, Faculty of Electrical Engineering and Information Technology, Universität der Bundeswehr München, Werner-Heisenberg-Weg 39, 85577 Neubiberg, Germany; marques@unibw.de

* Correspondence: michal.szulc@unibw.de

Abstract: Recent research trends show an increasing interest in non-equilibrium plasmas operated at atmospheric pressure, which are often used to tackle several environmental and health issues. Nevertheless, due to the complexity of the applications, these trends also show the need for a comprehensive characterization of such plasmas for a deeper understanding of the observed effects. One of the diagnostic methods for experimental determination of key parameters which affect the reactivity of a plasma, i.e., electron temperature, electron density and heavy particle temperature, is laser scattering. In this work, an approach based on a simple and compact laser scattering setup is proposed, which allows an estimation of the above parameters without any additional changes in the acquisition settings. Thus, the experimental effort and possible sources of error can be reduced. The proposed setup is tested experimentally with a commercially available pulsed plasma system, and the results are compared to available data. From this comparison, it is found that the plasma parameters estimated with the proposed scattering setup are plausible.

Keywords: plasma jet; low-current discharge; atmospheric pressure; laser scattering; electron density; electron temperature



Citation: Szulc, M.; Forster, G.; Marques-Lopez, J.-L.; Schein, J. A Simple and Compact Laser Scattering Setup for Characterization of a Pulsed Low-Current Discharge. *Appl. Sci.* **2022**, *12*, 6915. <https://doi.org/10.3390/app12146915>

Academic Editors: Mario De Cesare, Marilena Musto, Giuseppe Rotondo and Umberto Galietti

Received: 19 May 2022

Accepted: 6 July 2022

Published: 8 July 2022

Publisher's Note: MDPI stays neutral with regard to jurisdictional claims in published maps and institutional affiliations.



Copyright: © 2022 by the authors. Licensee MDPI, Basel, Switzerland. This article is an open access article distributed under the terms and conditions of the Creative Commons Attribution (CC BY) license (<https://creativecommons.org/licenses/by/4.0/>).

1. Introduction

The advantages of non-equilibrium plasmas at atmospheric pressure, such as high chemical reactivity [1,2] and low energy consumption [3,4], have ensured that such plasmas are now well established industrially and are steadily growing [5,6]. As a result, according to recent research trends [6–8], a comprehensive characterization of non-equilibrium plasmas is increasingly important, especially in the environmental and health application fields [2,9–12]. Non-equilibrium conditions in a plasma can be achieved in discharges driven by DC power supplies, but are commonly generated by a pulsed low-current high-voltage discharge [1,5,6,9], since the choice of the operating frequency as well as the shape of an excitation pulse makes the separate controllability of electron and heavy particle temperatures possible [1,13]. This enables a better adjustment of the plasma to the required application.

In general, the results of plasma treatments depend on the chemistry at the interface between the plasma and the treated object, which is governed by an interplay of the collision rates of energetic electrons and of ions with other particles or neutrals of the surrounding gas [1,14,15]. Because electrons can absorb more energy from the external electric field due to their high mobility compared to other plasma constituents, plasma chemistry is defined by electron number density n_e and electron temperature T_e [6,16]. As a result, if the electron number density is high, the ionization and dissociation reactions are driven by inelastic electron collisions. Nevertheless, these reactions can also be governed by inelastic atom and molecule collisions, depending on the conditions and the plasma carrier gas used [17–19]. Thus, the knowledge of the heavy particle temperature T_h is, in general, as important as the

knowledge of the electron parameters, i.e., n_e and T_e [20]. The estimation of the quantities n_e , T_e and T_h allows the assessment of the chemical reactivity of a plasma and thus a better control over the occurring reactions [6].

Laser scattering is one of several diagnostic methods to experimentally determine the plasma parameters, n_e , T_e and T_h . This diagnostic technique is neither limited by the assumption of equilibrium conditions [21,22], nor by the plasma composition, as both atomic and molecular plasmas can be investigated [23,24], nor by the operating pressure range [25,26]. Laser scattering not only provides a high spatial resolution [27,28], but also a high temporal resolution when the laser is synchronized with the pulse frequency of the power supply [29].

In order to experimentally estimate the plasma parameters by means of laser scattering, the intensity of the scattered signal, which is proportional to both the concentration of scattering species and to the intensity of the incident laser radiation [30], has to be high enough to be clearly detected by the diagnostic setup. The results also depend on the scattering angle, i.e., the angle between the wave vector of the incident radiation and the wave vector of the scattered radiation, as reported by Gregori et al. [31]. Thus, laser scattering has its limitations. According to [26,27], the main detection-limiting factors are the inherent plasma radiation and the stray light, i.e., the light scattered by the surroundings of the measurement volume and not by the particles inside the volume. Thus, the lowest electron density that can be determined with a diagnostic setup consisting of a laser, a spectrograph and a camera is in the range of 10^{18} m^{-3} [27]. Usually, at such low number densities, a mask is placed at the exit of the spectrograph to block the laser wavelength so that the detection sensitivity of the camera can be increased. However, the use of a blocking mask requires an intermediate image plane and thus another optical image on the detector. Furthermore, the laser blocking mask has to be removed to calibrate the setup or to measure the temperature of heavy particles if Rayleigh scattering is used for this purpose. A detailed description of setups using a blocking mask can be found in [21,27]. To improve the stray light rejection, the spectral resolution of experimental setups is often increased by coupling multiple spectrographs in series. Double grating [32] or even triple grating [21,28,33] spectrographs are most commonly used. The latter are proven to be highly effective for electron densities below 10^{20} m^{-3} and enable, due to the high spectral resolution, in most cases, a setup calibration or estimation of T_h without major modifications (both based on Raman scattering) [21,26,27,34].

Nonetheless, non-equilibrium plasmas can be also characterized with a simpler laser scattering setup. The wide dynamic range of modern detection devices should allow to detect both the Rayleigh and Thomson scattering signals with one and the same setting. Hence, the determination of plasma parameters should be possible, even without a laser blocking mask with an appropriate choice of components and under certain experimental conditions (discussed in the following). This would have the advantage that no physical change is made to the setup or the acquisition settings, thus reducing potential sources of error. In addition, a simple layout can be much more compact and mobile. Such a simple laser scattering setup working without a blocking mask is proposed in this paper.

In the next section, the theoretical considerations for a simplified scattering setup are discussed, followed by the description of the setup in Section 3. In Section 4, the proposed layout is applied to estimate the plasma parameters of a pulsed low-current high-voltage discharge operated at atmospheric pressure. A discussion of the results is presented in Section 5, followed by a conclusion.

2. Theoretical Considerations

The incident laser light, an electromagnetic wave, interacts with charged plasma particles. During the short laser pulse, the duration of which is in the range of 6 ns according to the specification of the laser used [35], the bound and free electrons are accelerated due to their small mass and high mobility, compared to other heavier species and follow the electric field of the incident wave. Thus, the electrons start to oscillate with the frequency of the incident radiation. This oscillation causes the electrons to emit

electromagnetic radiation like an oscillating electrical dipole. Depending on the energy of the incident radiation, several interaction mechanisms can be distinguished. These can be mainly divided into those in which some energy is transferred to (or gained from) the interacting particle (called inelastic scattering, in which the emitted radiation has a slightly different wavelength than the incident radiation) and those in which the total kinetic energy is conserved (elastic scattering, in which the emitted and incident radiation have the same wavelength). Elastic scattering of electromagnetic waves in the visible range can be divided into Rayleigh (short RyS) and Thomson (ThS) scattering processes. In the RyS process, photons of the incident radiation are scattered by bound electrons in the atoms/molecules, compared to free plasma electrons in the ThS process. From the recorded ThS signal, the electron density and electron temperature can be derived. In the case of inelastic scattering, when energy is transferred between the incident radiation and plasma particles, the process is called Raman scattering. If longer wavelengths than the incident radiation are observed in the recorded signal, then energy is transferred to the interacting plasma particles, and the process is referred to as Stokes Raman scattering. If a shift to shorter wavelengths can be observed, the internal energy of the scattering particles is reduced and the process is referred to as anti-Stokes Raman scattering. Additionally, since Raman scattering occurs on molecular gases, rotational and vibrational lines can be detected in the scattered signal. Thus, when working with molecular gases, attention should be paid to the rotational Raman lines, which occur in the same wavelength range as the Thomson scattered signal and can therefore influence the evaluated results [27]. A comprehensive description of the scattering processes can be found in the works of Evans and Katzenstein [36] as well as Sheffield [30] and Jackson [37]. For more application-oriented descriptions, refer to [26,27,38,39].

Regardless of the scattering mechanism, the mean scattered power \overline{dP}_s over a spectral frequency range $d\omega$ is a function of the total spectral distribution of the radiation scattered by (free or bound) electrons $s(\vec{k}, \omega)$ within the scattering volume V and, since the scattering depends on the electric field strength of the incident radiation, \overline{dP}_s is also a function of incident power P_i . Furthermore, the spectral distribution function $s(\vec{k}, \omega)$ depends on the scattering geometry, i.e., on the difference \vec{k} between the wave vector of the incident radiation \vec{k}_i and the wave vector of the scattered radiation \vec{k}_s as well as the difference ω between the angular frequencies of the incident (ω_i) and scattered (ω_s) radiation. The incident power P_i is distributed across an area A , which defines the scattering volume V , as shown in Figure 1. This volume results also from the observation through solid angle Ω since only a part of the scattering signal can be registered from the chosen viewing direction. Concluding, for the mean scattered power, it can be written [26,40]

$$\frac{\overline{dP}_s/(d\omega \Omega)}{P_i/A} = \sum n_q V s(\vec{k}, \omega). \tag{1}$$

with σ denoting the differential scattering cross section for the scattering mechanism being considered and n_q the density of the scattering particles. This scattering cross section can be understood as the probability that a light quantum of the incident radiation is scattered by a particle of the medium (i.e., the free and bound electrons) into the observation solid angle.

The variables \overline{dP}_s , σ , n_q and $s(\vec{k}, \omega)$ are specific for each scattering mechanism. In case of Thomson scattering, if incoherent scattering is assumed, the scattered signal is a sum of the uncorrelated contributions of each scattering particle and the spectral distribution function $s_{ThS}(\vec{k}, \omega)$ can be described by a Gaussian function [26]. Hence, it can be written as

$$s_{ThS,incoh}(\vec{k}, \lambda, \lambda_0) = s_{0,ThS} e^{-\left(\frac{\lambda-\lambda_0}{\Delta\lambda_{ThS}}\right)^2} \tag{2}$$

with

$$s_{0,ThS} = \frac{2\sqrt{\pi}c_0}{kv_{e,th}\lambda_0^2} \tag{3}$$

and

$$\Delta\lambda_{ThS} = \frac{kv_{e,th}\lambda_0^2}{2\pi c_0} \tag{4}$$

where λ_0 denotes the incident laser wavelength, c_0 the speed of light, k the absolute value of the difference between the wave vector of the scattered radiation \vec{k}_s and the wave vector of incident radiation \vec{k}_i and $v_{e,th}$ denotes the thermal electron velocity.

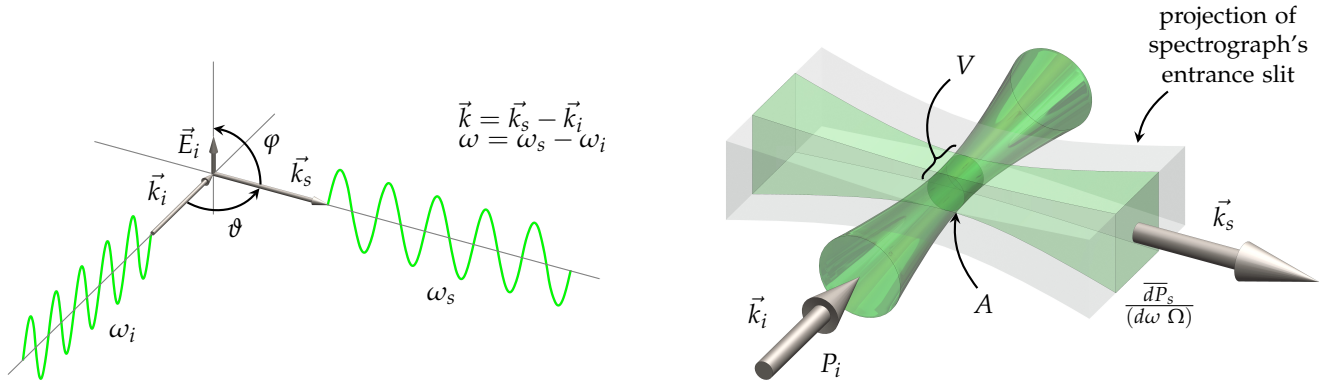


Figure 1. Scattering geometry used in this work. The angle $\varphi = 90^\circ$ is chosen to maximize the scattered intensity, whereas the scattering angle $\vartheta = 90^\circ$ is chosen to acquire an incoherent scattering signal. The incident power P_i of the laser beam is distributed across an area A , which defines the scattering volume V . The detection apparatus records the mean scattered power \overline{dP}_s over a spectral frequency range $d\omega$ observed through solid angle Ω .

The spectral distribution function does not in general correspond exactly to the experimentally measured scattering signal. The registered signal at (for instance) the detector, an image intensified charge coupled device (ICCD) camera, depends not only on the spectral sensitivity of the imaging sensor, but also on the sensitivity of the experimental setup and on the spectrometer’s transfer function. Hence, for the measured signal $M(\lambda^*)$, it can be written

$$M(\lambda^*) = K \int S(\lambda) S_F(\lambda - \lambda^*) d\lambda, \tag{5}$$

with $S(\lambda)$ as the scattered light spectrum, K as the detection sensitivity of the experimental setup and S_F denoting the transfer function of the setup. The detection sensitivity K takes into account the spectral response of all setup components, i.e., the spectral sensitivity of the ICCD, the lenses, mirrors and spectrometer used. Since the spectral range of the scattering signal is usually smaller than 20 nm [21,34,41], the sensitivity K is assumed to be independent of the wavelength and furthermore to be constant within this range. Both parameters, the detection sensitivity K and transfer function S_F , can be determined by measuring light scattered by a reference object (source) with known properties. Rayleigh scattering of pure nitrogen at room temperature and atmospheric pressure can be used for this purpose. Analogous to Equations (2)–(4), the main parameters determining the scattering spectrum are, in the case of the Rayleigh scattering mechanism, the temperature of heavy particles T_h and the heavy particle number density n_h , which for the above conditions can be obtained from the ideal gas law.

Since thermal equilibrium can be assumed for room temperature under atmospheric pressure conditions, the spectral line width of the Rayleigh scattered signal is in the range of picometers [42]. However, the resolution of the used spectrometer usually cannot resolve linewidths in the picometer range (see Section 3); hence, for the spectral distribution function of Rayleigh signal, a Dirac delta function can be assumed

$$s_{RyS}(\vec{k}, \lambda, \lambda_0) = s_{0,RyS} e^{-\left(\frac{\lambda - \lambda_0}{\Delta\lambda_{RyS}}\right)^2} \cong \delta(\lambda - \lambda_0). \tag{6}$$

According to the above discussion, the following relation can be written for the measured Rayleigh scattered signal by combining Equation (1) with Equations (5) and (6),

$$M_{RyS}(\lambda^*) = \sigma_R n_h V K \int \delta(\lambda - \lambda_0) S_F(\lambda - \lambda^*) d\lambda \tag{7}$$

or equivalently,

$$M_{RyS}(\lambda^*) = \sigma_R n_h V K S_F(\lambda^*). \tag{8}$$

Assuming that the transfer function $S_F(\lambda^*)$ is normalized to 1, the above equation can be solved for the detection sensitivity K in the case of $\lambda^* = \lambda_0$ and yields

$$K = \frac{M_{RyS}(\lambda^* = \lambda_0)}{\sigma_R n_h V}. \tag{9}$$

Accordingly, the transfer function of the whole detection apparatus, which is mainly determined by the transfer function of the spectrometer, is given by

$$S_F(\lambda^*) = \frac{M_{RyS}(\lambda^*)}{\sigma_R n_h V K}. \tag{10}$$

With both the detection sensitivity K and transfer function S_F defined based on the Rayleigh scattering signal, the spectral distribution of the measured Thomson scattering signal $M_{ThS}(\lambda^*)$ can be expressed similarly to Equation (7) as

$$M_{ThS}(\lambda^*) = \sigma_T n_e V K \int s_{0,ThS} e^{-\left(\frac{\lambda - \lambda_0}{\Delta\lambda_{ThS}}\right)^2} S_F(\lambda - \lambda^*) d\lambda. \tag{11}$$

The substitution of Equation (9) for K yields

$$M_{ThS}(\lambda^*) = \frac{\sigma_T n_e}{\sigma_R n_h} M_{RyS}(\lambda^* = \lambda_0) \int s_{0,ThS} e^{-\left(\frac{\lambda - \lambda_0}{\Delta\lambda_{ThS}}\right)^2} S_F(\lambda - \lambda^*) d\lambda. \tag{12}$$

If the spectral width of the transfer function S_F is significantly smaller than the spectral width of the Thomson scattered spectrum $s_{0,ThS}$, then the convolution integral, which represents the spectral distribution of the measured signal M_{ThS} , is accurately reproduced by a Gaussian distribution function. Hence,

$$\int s_{0,ThS} e^{-\left(\frac{\lambda - \lambda_0}{\Delta\lambda_{ThS}}\right)^2} S_F(\lambda - \lambda^*) d\lambda = m_{0,ThS} e^{-\left(\frac{\lambda^* - \lambda_0}{\Delta\lambda_{m,ThS}}\right)^2}. \tag{13}$$

Thereafter, the electron temperature T_e can be determined from the characteristic width $\Delta\lambda_{m,ThS}$ of the measured signal fitted by a Gaussian curve. The electron density n_e , on the other hand, can be determined by rearranging the Equation (12) to

$$n_e = \frac{M_{ThS}(\lambda^* = \lambda_0)}{M_{RyS}(\lambda^* = \lambda_0)} \frac{\sigma_R}{\sigma_T} n_h \frac{1}{m_{0,ThS}}. \tag{14}$$

The heavy particle temperature, on the other hand, is determined from the intensity ratio of the Rayleigh peaks of the cold gas and plasma measurements via the ideal gas law after the respective measurements have been corrected for stray light beforehand (discussed in detail in Section 3). This is possible because the recorded Rayleigh scattered intensity is directly proportional to the particle density according to the Equation (8).

According to the above considerations, the choice of the spectrograph is a key point for an accurate functioning of the proposed method. Its spectral resolution should be significantly smaller than the spectral width of the Thomson scattered signal, but low enough to satisfy the assumption of a Dirac delta function for the Rayleigh signal. These requirements are easily achievable with most of today's instruments. Under these conditions,

the setup can be calibrated with the Rayleigh signal. If then the electron number density of the measurement object is high enough so that a sufficient intensity of the Thomson signal can be detected and the stray light, i.e., the light scattered by the immediate vicinity of the measurement volume, is low, a measurement can be performed with constant acquisition settings.

Influence of Rotational Raman Scattering

As briefly mentioned in the beginning of this section, the spectral ranges of Thomson scattering and rotational Raman scattering signals overlap. Hence, the influence of the latter on the results should be evaluated. According to Narishige et al. [32], an overlap occurs when the total density of the Raman scattering particles n_j is 10^4 times larger than electron density, since Raman scattering cross sections are about 10^{-5} times smaller than the Thomson scattering cross section at the used laser wavelength. If the spectral distribution of the measured Raman signal $M_{RaS}(\lambda^*)$ is expressed similarly to Equation (12), both $M_{ThS}(\lambda^*)$ and $M_{RaS}(\lambda^*)$ signals can be put into relation as they are calibrated with the Rayleigh scattering signal $M_{RyS}(\lambda^* = \lambda_0)$. Since the Raman spectrum for a given plasma gas at a specific temperature of heavy particles can be calculated if the instrumental profile of the detection apparatus is known, as described in [26], the influence of rotational Raman scattering can be estimated by comparing the experimentally measured signals of $M_{RyS}(\lambda^*)$ and $M_{ThS}(\lambda^*)$ with the calculated $M_{RaS}(\lambda^*)$ signal. Such a comparison is presented in Figure 2 for nitrogen, which is used in this work.

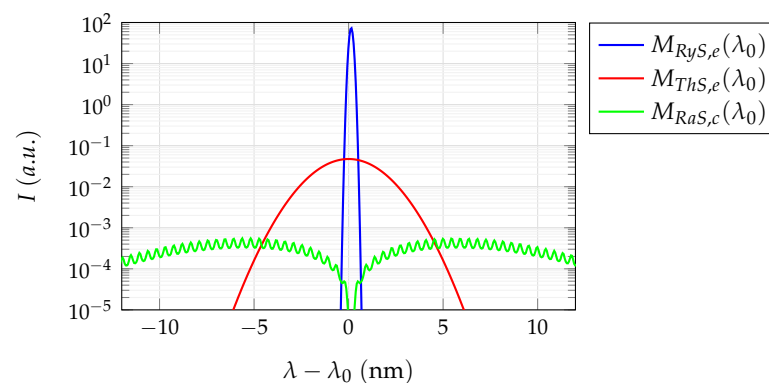


Figure 2. Comparison of intensities of the Rayleigh $M_{RyS,e}(\lambda_0)$ and Thomson $M_{ThS,e}(\lambda_0)$ signals measured for a pulsed, low-current nitrogen discharge and the calculated Raman $M_{RaS,c}(\lambda_0)$ spectra. The heavy particle temperature needed for the calculation of $M_{RaS,c}(\lambda_0)$ is determined from the experimentally measured $M_{RyS,e}(\lambda_0)$ and $M_{ThS,e}(\lambda_0)$ signals and amounts to $T_h = 3500$ K.

From the experimentally measured $M_{RyS,e}(\lambda_0)$ and $M_{ThS,e}(\lambda_0)$ signals, a heavy particle temperature of 3500 K was determined for a pulsed, low-current nitrogen discharge operated at atmospheric pressure (described in Section 3.1). The $M_{RaS}(\lambda^*)$ signal was then calculated for this temperature and compared with the experimentally measured signals. As can be seen in Figure 2, the measured Thomson scattering signal is three orders of magnitude smaller than the measured Rayleigh signal, whereas the calculated rotational Raman spectrum is approximately two orders of magnitude smaller than the Thomson signal. Taking into account that the intensity of the $M_{RaS,c}(\lambda_0)$ signal decreases with increasing T_h , while the spectral range becomes broader [26], it can be assumed that the rotational Raman signal does not significantly influence the Thomson scattering signal and hence the determined plasma parameters for the experimental setup proposed in the next section.

3. Experimental Setup

The implementation of the proposed method, similarly to other scattering techniques, requires the usage of a high power light source [38]. In this work, a Nd:YAG pulse laser of type Surelite SL II-10 made by Continuum, Santa Clara, CA, USA, is used. Coupled with

a frequency doubler of type SSP-2, also produced by Continuum, pulses with a central wavelength of $\lambda_0 = 532$ nm and a width of 4–6 ns are generated [35]. As schematically presented in Figure 3, the initial laser beam is diverted by 180° using two mirrors with a high laser damage threshold and a diameter of 50 mm and focused on the scattering volume using a planoconvex lens with a focal length of 500 mm and a diameter of 50 mm. This allows for a compact setup. To ensure the recording of the highest possible intensity of the scattered signal, the laser beam is polarized vertically and is perpendicular to the propagation direction of the scattered wave, while the scattering plane is chosen to be horizontal and also perpendicular to the beam polarization. Such “square” setups are recommended for plasmas with low electron densities [43] and are most commonly used in experiments [21,26,34]. A Fastie–Ebert spectrograph made by Garching Instrumente GmbH, Munich, Germany, with a focal length of 250 mm is chosen for the detection apparatus, coupled with an ICCD camera of type 4 Picos from Stanford Computer Optics, Berkeley, CA, USA, positioned in the image plane of the spectrometer. As shown in Figure 3, the scattered beam is projected onto the horizontally oriented entrance slit by a planoconvex lens with a focal length of 100 mm coupled with a diaphragm to control the solid angle of the beam. The moderate focal length of the spectrograph combined with a diffraction grating of 1500 L/mm operated in the first diffraction order yields an aperture of $f/4$. The image intensifier of the camera, a Gen II photo-cathode of type S20 with a single-stage microchannel plate and a P43 phosphor screen optically coupled via an internal, distortion-free $f/0.8$ lens to a CCD chip with a resolution of 768×576 px, offers a quantum efficiency of about 11% at a wavelength of 532 nm [44]. Moreover, the ICCD camera is triggered externally so that it can be synchronized with the laser pulse and the discharge pulses. Additionally, the PG31 plasma generator is mounted on a motorized XYZ positioning unit, which simplifies adjustment and allows reproducible positioning during the experiments.

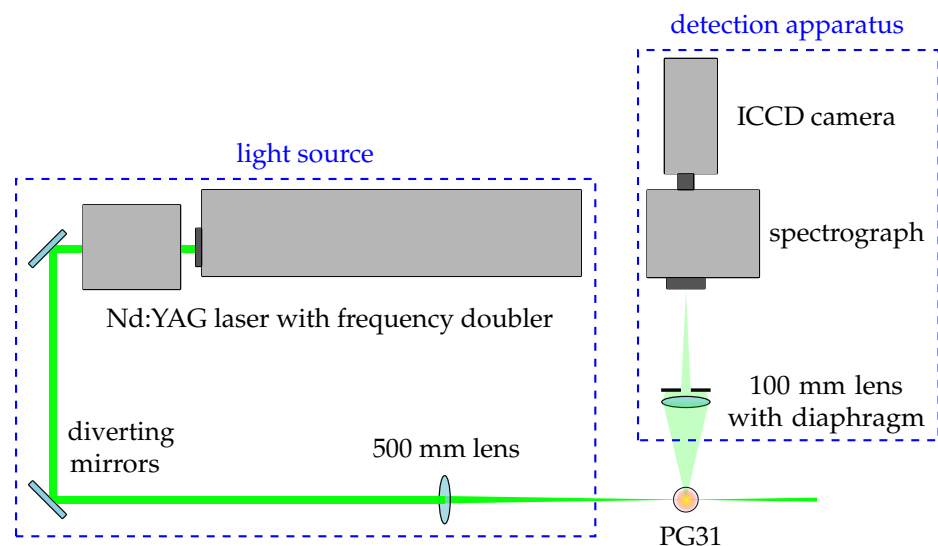


Figure 3. Schematic diagram of the experimental setup for laser scattering (not to scale). The entrance slit of the spectrograph is oriented horizontally.

The setup depicted in Figure 3 is operated in sampling mode, with the laser pulse and camera triggered at maximum amplitude of the current pulse. To synchronize the laser pulse frequency with the operating frequency of the power supply, a slightly modified triggering circuit from [45] was used. The input of the pulse-delay generator DG645 from Stanford Research Systems, Sunnyvale, CA, USA, was set to block the incoming trigger edges for a period of 100 ms, thus ensuring the required laser pulse frequency of 10 Hz. The gain voltage of the ICCD was set to 800 V, resulting in a good signal-to-noise ratio without saturation of the most intense Rayleigh signal. Most of the stray light is caused by backward reflection of the laser along its direction of incidence. This can be reduced significantly by

temporal discrimination if the reflection point is suitably far away from the scattering point, i.e., by selecting a sufficiently short exposure time of the detection apparatus [21,46,47]. Hence, considering the laboratory conditions and the jitter due to external triggering (see Section 3.1), an exposure time of 15 ns was set for the experiments. Both camera settings were kept constant for all following experiments. A spectral resolution of 0.055 nm/px was obtained for the detection apparatus with a neon spectral calibration lamp of type 6032 made by Oriol Instruments, Stratford, CT, USA, with the entrance slit width of the spectrograph set to 150 μm . The full width at half maximum of the instrumental profile for the above settings amounts hereby to 0.22 nm. Furthermore, the spatial resolution of the setup amounts to 0.041 mm/px. Taking into account the length of the focal point of the laser beam, i.e., the length of the measurement volume, the region of interest in the acquired images is expected to be 50 px or less wide. Because the region of interest is small compared to the width of the whole image, several aberrations exhibited by the simple Fastie–Ebert design as well as the curved focal field [48] are neglected.

Although precautions are taken to minimize stray light, it cannot be completely eliminated by temporal discrimination because the incident laser light is also scattered by objects or surfaces in direct vicinity of the measurement volume, such as the metallic surface of the nozzle tip. However, this stray light can be estimated by comparing the measured scattering intensity on nitrogen with an additional measurement of scattering on helium [22,26,49]. Since the ground state of helium has one of the smallest scattering cross sections [21,50], an assumption is thus made under atmospheric conditions, that the detected intensity is only due to reflections from the surrounding objects. Thereafter, the measurement procedure consists of three steps. For better understanding, the average images resulting from each step are shown in Figure 4. First, since the discharge is operated at atmospheric pressure, the stray light is evaluated by measurement of the scattered intensity on helium flowing through the generator (Figure 4a). The discharge is switched off in this step. In the second step, a cold gas measurement is performed to obtain a calibration profile of the scattering setup (Figure 4b). During this step, pure nitrogen flows through the generator without the plasma being ignited. Accordingly, the acquired images, at least 1500 for each measurement, contain a Rayleigh scattering signal as well as the stray light from the surfaces surrounding the measurement volume. Finally, a measurement is performed with the discharge switched on (Figure 4c). The signal registered in this step consists of a Rayleigh scattering signal, a Thomson scattering signal and the stray light. All of the above measurements need to be pre-processed before evaluation of the plasma parameters. The invalid images, mainly due to Mie scatterers caused by dust and other particles in ambient air, are sorted out, and a mean image is calculated from the valid images. Before the evaluation, which is done pixel line by pixel line, the background intensity is subtracted from each selected pixel line of the respective average image to correct for any differences in the dark current of the ICCD camera. Thereafter, the selected pixel line of the average stray light image is subtracted from the corresponding pixel line of the other images. As a result, the pure Rayleigh scattered signal is obtained from the average cold gas image and a Thomson and Rayleigh scattered signal from the average plasma image. These two signals are subsequently used to determine the plasma properties, as theoretically described in Section 2. A sample Thomson scattering signal extracted for a single pixel line is presented in Figure 4d.

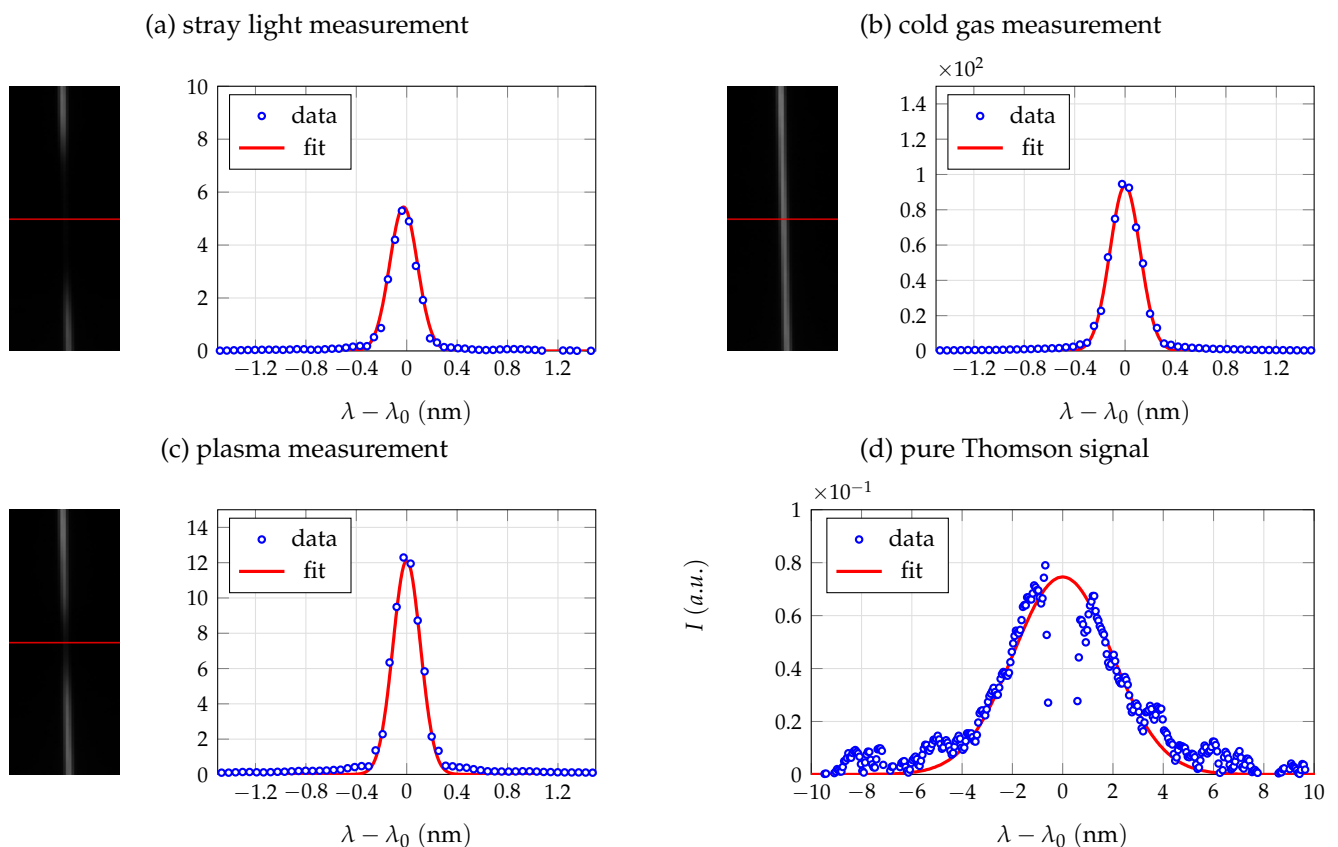


Figure 4. Average images of (a) stray light, (b) cold gas, and (c) plasma measurements obtained after pre-processing, and the corresponding spectral profiles for the marked pixel line used to determine the plasma parameters. The pure Thomson scattering signal extracted from these spectral profiles is shown in diagram (d).

3.1. Test Object

A commercially available pulsed plasma system, using a comparable working principle to that of other systems on the market [51–54], is chosen to test the proposed scattering setup. The system consisting of a PG31 plasma generator and a PS2000 OEM power supply is produced by Relyon Plasma GmbH, Regensburg, Germany. Its main application fields are surface activation, decontamination or deposition of different materials [53,55–58].

The PG31 generator has a conventional construction with a positively biased, finger-shaped non-refractory inner electrode and a copper alloy nozzle acting as cathode. Several nozzle geometries are available from the manufacturer—a conical shaped one of type A450 with an outlet diameter of 4 mm is used exclusively for the investigations. The generator is optimized for operation with molecular gases and gas flow rates between 35–60 standard liters per minute (short L/min) [56]. Accordingly, pure nitrogen at a flow rate of 35 L/min is used in the following experiments, regulated externally by a mass flow controller of type 8626 produced by Bürkert GmbH & Co. KG, Ingelfingen, Germany. The effluent plasma jet operating at 60 kHz can be seen in Figure 5.

The discharge is driven by unipolar, triangular current pulses with variable amplitude of maximal 1 A generated at the output of the PS2000 power supply. The power supply utilizes a single-phase full-bridge push-pull converter design with the rise and fall times of the triangular pulses fixed at 5 μ s, regardless of the selected pulse frequency. The power supply can be controlled via a PC software and allows an adjustment of the output power between 70% and 100%, which corresponds to a current amplitude of 0.7–1.0 A at the exit, whereas the pulse frequency can be varied between 40 kHz and 65 kHz in 1 kHz steps. In the experiments, the power setting was set to 100% (i.e., current amplitude of 1.0 A) and

the operating frequency to 60 kHz. The typical current and voltage traces for these settings are presented in Figure 6.

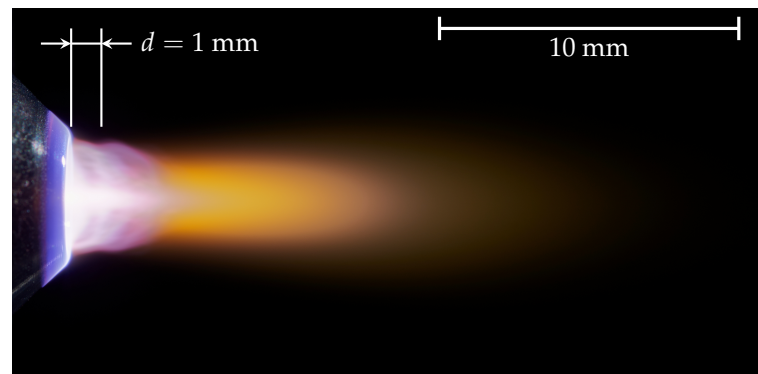


Figure 5. The effluent plasma jet of a PG31 generator equipped with an A450 nozzle, showing the axial distance $d = 1$ mm at which the measurements were performed.

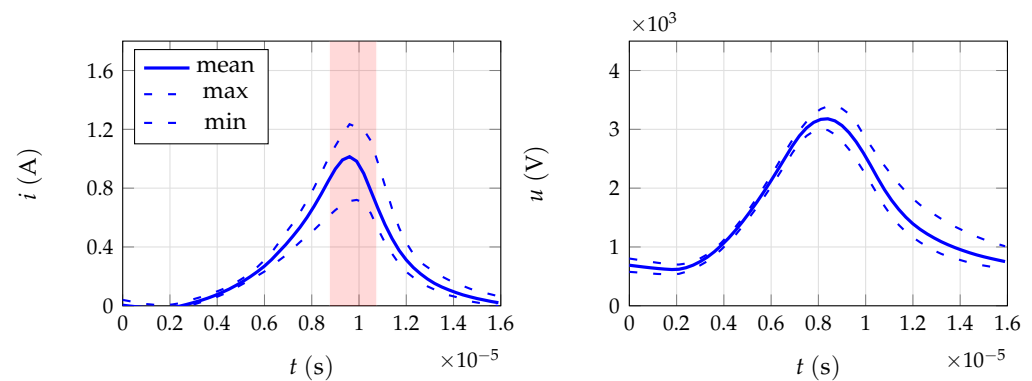


Figure 6. Typical voltage and current traces recorded for a frequency of 60 kHz and a power setting of 100%. The trigger timeframe at which the experimental setup was triggered is marked in the current plot.

4. Results

To test the proposed setup, the relevant plasma parameters of a pulsed low-current plasma jet were determined. Before the study was started, the radial position of the plasma generator was adjusted so that the incident laser beam passes exactly through the generator axis. Thereafter, the generator was positioned so that the incident laser beam passed under the nozzle outlet at a downstream axial distance d of 1 mm, as marked in Figure 5. A total of 8 measurements at that axial distance were made and subsequently evaluated.

The average radial distribution of the estimated parameters is presented in Figure 7. It became apparent that for the chosen parameter set, electron parameters can be reliably estimated for a radial distance r perpendicular to the jet axis of 0.7 mm. As depicted in Figure 7, the estimated electron number density varies by about $0.7 \times 10^{21} \text{ m}^{-3}$ between the jet axis and the outer fringes at radii above 0.6 mm, an increase of slightly more than 30%. It should be noted that the maximum value of $2.3 \times 10^{21} \text{ m}^{-3}$ is reached about 0.1 mm outside the axis. Looking at the error bars, a deviation of 25% from the average n_e value is to be expected throughout the analyzed diameter. In contrast, no significant increase in the electron temperature with varying radius is observed. A mean T_e value of 41,000 K is estimated with a similar deviation of about 25%. The temperature of heavy particles in turn shows a significant, Gaussian-like radial distribution with a maximum value of 5800 K lying at the jet axis and a negative gradient of $\sim 3000 \text{ K/mm}$ toward larger distances from the axis. Additionally, an approximately 0.2 mm wide temperature plateau can be observed centered around the axis, as marked in Figure 7. Analogous to other plasma parameters,

the standard deviation of T_h also ranges about 25%, although a decrease with increasing radius can be observed. The increased standard deviation of T_h about the jet axis, as well as the asymmetric behavior (different error values for positive and negative r -values), appear to be caused by a slight lateral movement of the discharge channel from one measurement to the other and are amplified by the averaging. The latter effect was also observed to some extent in the raw data for the electron parameters, in particular, n_e , but is much less pronounced than for T_h .

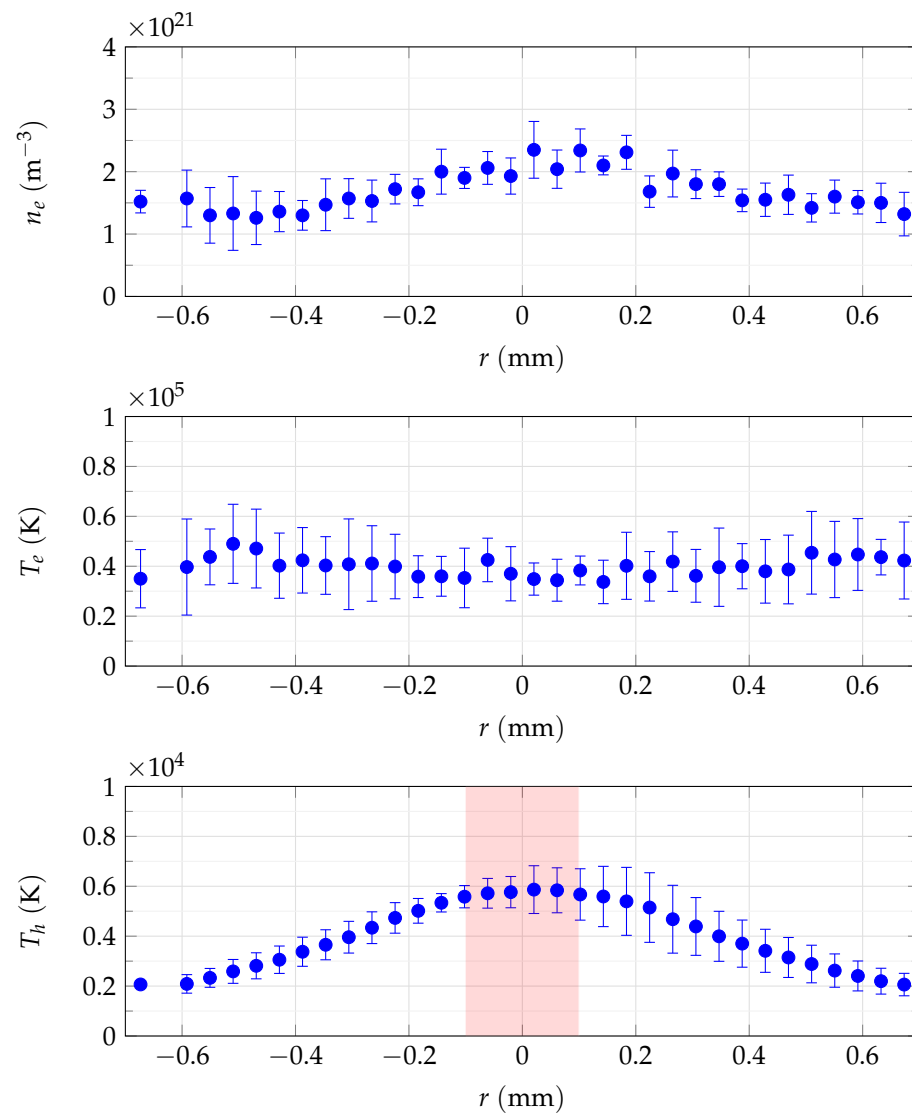


Figure 7. Plasma parameters (n_e , T_e , T_h) estimated from scattering measurements at an axial distance of $d = 1$ mm for a pulse frequency of 60 kHz and a power setting of 100% of the system under study.

5. Discussion of the Results

To check the plausibility of the results shown in Figure 7, they are compared in the following with reference values determined experimentally or by calculations for low-current discharges operated at atmospheric pressure, although some of the experimental setups in those references do not correspond to the experiment considered in this work. The most relevant references are summarized in Table 1.

According to Reece Roth [59], electron densities ranging between 10^{20} m⁻³ and 10^{21} m⁻³ and heavy particle temperatures below 5800 K can be expected for discharges driven by a constant current of less than 50 A, which is in good agreement with the values estimated in this work. In comparison to that, the electron temperature reported in [59]

is significantly lower than that estimated in this work. It should be noted, however, that the operating frequency is quite different—the values presented in [59] are determined for direct current (constant energy supply), while the generator studied in this work is pulsed at frequencies in the range of 50 kHz. Therefore, the discrepancy may be correlated with the operating frequency of the discharge under study.

As presented by Kruger et al., a significantly higher electron temperature is required to achieve a similar electron density in pulsed operation as is the case for a discharge driven by direct current [4]. This suggestion that the relatively high electron temperature is related to the pulsed nature of the discharge, is confirmed in further references, where pulsed discharges were studied [60–63]. Subsequently, Pai et al. determined an electron temperature of about 30,000 K and an electron density value of about 10^{21} m^{-3} for a discharge of nanosecond duration driven in air by 8.3 kV high voltage peaks pulsed at 30 kHz [61,62]. For these working conditions, peak current values of 30 A were measured, resulting in a rotational temperature of 5300 K, reached about 40 ns after a discharge took place. The heavy particle temperature was determined by fitting synthetic spectra to the SPS (0,0)-transition. Both the electron density and temperature on the other hand were estimated based on calculations of the discharge radius and collision frequency between electrons and heavy particles [61]. Although the reported electron temperature is somewhat lower according to Table 1, the values determined by Pai et al. concur well with the results estimated in this work.

Table 1. Comparison of the scattering results with the most relevant reference values.

Ref.	This Work	[59]	[61,62]	[64]
Gas	N ₂	–	Air	N ₂
<i>f</i> (kHz)	60 kHz	DC	30 kHz	DC
<i>i</i> (A)	~1 (peak)	<50	30 (peak)	0.23
\bar{n}_e (m ⁻³)	~2 × 10 ²¹	<10 ²¹	1.0 × 10 ²¹	1.6 × 10 ²¹
\bar{T}_e (K)	41,000	<23,000	30,000	–
\bar{T}_h (K)	5900	<5800	5300	~6000

The higher T_e and n_e values observed in this work are correlated not only with the operating frequency, but probably also with the plasma gas used. Molecular gases, especially nitrogen, are capable of accumulating energy in vibrational, metastable or dissociated states over longer periods of time [17,18]. Reactions such as ionic recombination or metastable-induced dissociation (that can lead to the creation of secondary electrons), neutral interactions, and diffusion processes occur in nitrogen plasmas on timescales of hundreds of microseconds or even milliseconds [1,65,66]. Hence, the high temperature and concentration of excited species within the discharge channel cannot be cleared fast enough by the gas flow when operating at sufficiently high pulse repetition rates [67], where the recombination time scale and the inverse of the pulse frequency are similar to each other. At a pulse frequency in the range of 50 kHz, the time period (~20 μs) between successive energy pulses lies in the same order of magnitude as the recombination time of nitrogen species and therefore an appreciable deviation of electron parameters from the steady state achieved under direct current is to be expected.

Almost identical electron density as well as heavy particle temperature values compared to those estimated in this work, were reported in recent investigations of gliding arcs constricted by tubes, referred to as gliding arc plasmatron by Gröger et al. [64] or tornado discharge by researchers collaborating with Gutsol and Fridman [68]. A gliding arc is, in its simplest form, a discharge ignited in a transversal gas flow between two divergent electrodes. Due to the movement of the discharge along the electrodes caused by the gas flow, such discharge is often referred to as self-pulsating, even though it is driven with a direct current [69–71]. As presented in Table 1, Gröger et al. operated the plasmatron with nitrogen at a constant current of 230 mA [64]. The rotational and vibrational temperatures of about 6000 K were estimated by synthetic spectra fitting after measuring of the SPS

(0,0)- and FNS (0,0)-transitions of molecular nitrogen. Similar to [61,62], the authors also determined the reduced electric field based on spectroscopic measurements and used it to calculate the electron density with a collisional–radiative model of the discharge. The resulting n_e was estimated to be $1.6 \times 10^{21} \text{ m}^{-3}$ [64]. This value may be higher than reported by others for gliding arcs [69–71], but according to the observations of Machala et al. [72], the increase in electron density is most probably caused by the constriction of the discharge. Both n_e and T_h values given in [64] are in good agreement with the ones determined in this work. Gröger et al. did not state any T_e values.

The plateau width of 0.2 mm observed in the radial distribution of T_h in Figure 7 is considered to be the core diameter of the discharge channel. This assumption appears to be correct when the diameter is compared with other works. Pai et al. estimated a diameter of about 0.3 mm for the nanosecond pulsed discharge discussed above [61]. This compares to the core diameter estimated by Gröger et al. of about 0.5 mm [64]. According to radial temperature profiles given by Lebouvier et al., who modeled a low-current high-voltage DC plasma jet operated with a constant current in the range of 0.5 A and an air flow rate of 25 L/min in [73], the diameter of the discharge channel at the nozzle outlet is about 0.4 mm.

Apart from the references summarized in Table 1, several research groups analyzed plasma systems comparable to the one studied here [51,53,74–77], though only few have determined the temperature of the effluent plasma jet using emission spectroscopy. Kubota et al. spectroscopically analyzed a comparable plasma system operated at a pulse frequency of 19 kHz, with nitrogen flowing at 30 L/min [74]. Based on the second positive (0,0)-transition, the rotational temperature was estimated to be about 5000 K inside the plasma generator and between 3000 K and 4000 K at nozzle exit. For the same plasma system, also pulsed at 19 kHz but working with a compressed air gas flow rate of 76.6 L/min, Dowling et al. estimated a rotational temperature of about 1760 K at nozzle exit using the (0,2)-transition spectra of the second positive system of molecular nitrogen [51]. If in a first approximation for this result a linear relationship between gas flow and temperature would be assumed, than a rotational temperature of approx. 4500 K at an air flow rate of 30 L/min could be expected. Both results agree well with the T_h values estimated in this work under the assumption that $T_h = T_{rot}$.

6. Conclusions and Outlook

To conclude, based on the above discussion, it can be stated that the estimated plasma parameters are plausible. The simple, compact and mobile laser scattering setup proposed in this work has proven to be well suited for determination of electron parameters in transient non-equilibrium plasmas at atmospheric pressure. The choice of components allow the plasma parameters to be measured without changing the setup or acquisition settings, thereby reducing the potential risk of error. Consequently, the spatial distribution of n_e , T_e and T_h for different operating frequencies or power settings of the plasma system can be determined in the next step. With an appropriate synchronization of the setup with the pulse frequency, the temporal change of the parameters can also be determined.

Author Contributions: Conceptualization, M.S., G.F. and J.S.; methodology, M.S. and G.F.; software, G.F.; validation, M.S.; formal analysis, J.-L.M.-L. and J.S.; investigation, M.S.; resources, M.S. and G.F.; data curation, M.S. and J.-L.M.-L.; writing—original draft preparation, M.S.; writing—review and editing, J.-L.M.-L. and J.S.; visualization, M.S.; supervision, J.S.; project administration, M.S.; funding acquisition, J.S. All authors have read and agreed to the published version of the manuscript.

Funding: This research received no external funding.

Institutional Review Board Statement: Not applicable.

Informed Consent Statement: Not applicable.

Data Availability Statement: Not applicable.

Acknowledgments: The publication of this manuscript was financially supported by Universität der Bundeswehr München.

Conflicts of Interest: The authors declare no conflict of interest.

Abbreviations

The following abbreviations are used in this manuscript:

CCD	Charge-coupled device
ICCD	Intensified charge-coupled device
RyS	Rayleigh scattering
ThS	Thomson scattering

References

1. Bruggeman, P.J.; Iza, F.; Brandenburg, R. Foundations of atmospheric pressure non-equilibrium plasmas. *Plasma Sources Sci. Technol.* **2017**, *26*, 123002. [[CrossRef](#)]
2. Snoeckx, R.; Bogaerts, A. Plasma technology—A novel solution for CO₂ conversion? *Chem. Soc. Rev.* **2017**, *46*, 5805–5863. [[CrossRef](#)] [[PubMed](#)]
3. Hsu, C.C.; Wu, C.Y. Electrical characterization of the glow-to-arc transition of an atmospheric pressure pulsed arc jet. *J. Phys. D Appl. Phys.* **2009**, *42*, 215202. [[CrossRef](#)]
4. Kruger, C.H.; Laux, C.O.; Yu, L.; Packan, D.M.; Pierrot, L. Nonequilibrium discharges in air and nitrogen plasmas at atmospheric pressure. *Pure Appl. Chem.* **2002**, *74*, 337–347. [[CrossRef](#)]
5. Bogaerts, A.; Neyts, E.; Gijbels, R.; van der Mullen, J.J.A.M. Gas discharge plasmas and their applications. *Spectrochim. Acta B* **2002**, *57*, 609–658. [[CrossRef](#)]
6. Weltmann, K.D.; Kolb, J.F.; Holub, M.; Uhrlandt, D.; Šimek, M.; Ostrikov, K.K.; Hamaguchi, S.; Cvelbar, U.; Černák, M.; Locke, B.; et al. The future for plasma science and technology. *Plasma Process. Polym.* **2019**, *16*, 1800118. [[CrossRef](#)]
7. Kim, Y. Exploring emerging technologies with analysis of bibliographic data focused on plasma surface treatment. *Coatings* **2021**, *11*, 1291. [[CrossRef](#)]
8. Cvelbar, U.; Walsh, J.L.; Černák, M.; de Vries, H.W.; Reuter, S.; Belmonte, T.; Corbella, C.; Miron, C.; Hojnik, N.; Jurov, A.; et al. White paper on the future of plasma science and technology in plastics and textiles. *Plasma Process. Polym.* **2017**, *16*, 1700228. [[CrossRef](#)]
9. Aggelopoulos, C.A. Recent advances of cold plasma technology for water and soil remediation: A critical review. *Chem. Eng. J.* **2022**, *428*, 131657. [[CrossRef](#)]
10. Mai-Prochnow, A.; Zhou, R.; Zhang, T.; Ostrikov, K.K.; Mugunthan, S.; Rice, S.A.; Cullen, P.J. Interactions of plasma-activated water with biofilms: Inactivation, dispersal effects and mechanisms of action. *NPJ Biofilms Microbiomes* **2021**, *7*, 11. [[CrossRef](#)]
11. Machala, Z.; Tarabová, B.; Sersenová, D.; Janda, M.; Hensel, K. Chemical and antibacterial effects of plasma activated water: correlation with gaseous and aqueous reactive oxygen and nitrogen species, plasma sources and air flow conditions. *J. Phys. D Appl. Phys.* **2019**, *52*, 034002. [[CrossRef](#)]
12. Zeghioud, H.; Nguyen-Tri, P.; Khezami, L.; Amrane, A.; Assadi, A.A. Review on discharge plasma for water treatment: mechanism, reactor geometries, active species and combined processes. *J. Water Process. Eng.* **2020**, *38*, 101664. [[CrossRef](#)]
13. Lu, X. Effects of gas temperature and electron temperature on species concentration of air plasmas. *J. Appl. Phys.* **2007**, *102*, 033302. [[CrossRef](#)]
14. Dorai, R.; Kushner, M.J. A model for plasma modification of polypropylene using atmospheric pressure discharges. *J. Phys. D Appl. Phys.* **2003**, *36*, 666–685. [[CrossRef](#)]
15. Tanaka, Y. Time-dependent two-temperature chemically non-equilibrium modelling of high-power Ar-N₂ pulse-modulated inductively coupled plasmas at atmospheric pressure. *J. Phys. D Appl. Phys.* **2006**, *39*, 307–319. [[CrossRef](#)]
16. Muraoka, K.; Maeda, M. *Laser-Aided Diagnostics of Plasmas and Gases*; Series in Plasma Physics; Institute of Physics Publishing: Bristol, UK, 2001.
17. Akishev, Y.; Grushin, M.; Karalnik, V.; Petryakov, A.; Trushkin, N. Non-equilibrium constricted dc glow discharge in N₂ flow at atmospheric pressure: Stable and unstable regimes. *J. Phys. D Appl. Phys.* **2010**, *43*, 075202. [[CrossRef](#)]
18. Akishev, Y.; Grushin, M.; Karalnik, V.; Petryakov, A.; Trushkin, N. On basic processes sustaining constricted glow discharge in longitudinal N₂ flow at atmospheric pressure. *J. Phys. D Appl. Phys.* **2010**, *43*, 215202. [[CrossRef](#)]
19. Benilov, M.S.; Naidis, G.V. Modelling of low-current discharges in atmospheric-pressure air taking account of non-equilibrium effects. *J. Phys. D Appl. Phys.* **2003**, *36*, 1834–1841. [[CrossRef](#)]
20. Wang, W.Z.; Rong, M.Z.; Yan, J.D.; Murphy, A.B.; Spencer, J.W. Thermophysical properties of nitrogen plasmas under thermal equilibrium and non-equilibrium conditions. *Phys. Plasmas* **2011**, *18*, 113502. [[CrossRef](#)]
21. Hübner, S.; Santos Sousa, J.; Graham, W.G.; van der Mullen, J.J.A.M. Thomson scattering on non-thermal atmospheric pressure plasma jets. *Plasma Sources Sci. Technol.* **2015**, *24*, 054005. [[CrossRef](#)]
22. Murphy, A.B. Laser-scattering temperature measurements of a free-burning arc in nitrogen. *J. Phys. D Appl. Phys.* **1994**, *27*, 1492–1498. [[CrossRef](#)]
23. Kühn-Kauffeldt, M.; Marques, J.L.; Forster, G.; Schein, J. Electron temperature and density measurement of tungsten inert gas arcs with Ar-He shielding gas mixture. *J. Instrum.* **2013**, *8*, C10017. [[CrossRef](#)]

24. Thalman, R.; Zarzana, K.J.; Tolbert, M.A.; Volkamer, R. Rayleigh scattering cross-section measurements of nitrogen, argon, oxygen and air. *J. Quant. Spectrosc. Radiat. Transf.* **2014**, *147*, 171–177. [[CrossRef](#)]
25. Muraoka, K.; Kono, A. Laser Thomson scattering for low-temperature plasmas. *J. Phys. D Appl. Phys.* **2011**, *44*, 043001. [[CrossRef](#)]
26. van de Sande, M.J. Laser Scattering on Low Temperature Plasmas: High Resolution and Stray Light Rejection. Ph.D. Thesis, Technische Universiteit Eindhoven, Eindhoven, The Netherlands, 2002.
27. van Gessel, A.F.H.; Carbone, E.A.D.; Bruggeman, P.J.; van der Mullen, J.J.A.M. Laser scattering on an atmospheric pressure plasma jet: Disentangling Rayleigh, Raman and Thomson scattering. *Plasma Sources Sci. Technol.* **2012**, *21*, 015003. [[CrossRef](#)]
28. Kono, A.; Iwamoto, K. High-spatial-resolution multichannel Thomson scattering measurements for atmospheric pressure microdischarge. *Jpn. J. Appl. Phys.* **2004**, *43*, L1010. [[CrossRef](#)]
29. Zhu, J.; Ehn, A.; Gao, J.; Kong, C.; Aldén, M.; Salewski, M.; Leipold, F.; Kusano, Y.; Li, Z. Translational, rotational, vibrational and electron temperatures of a gliding arc discharge. *Opt. Express* **2017**, *25*, 20243–20257. [[CrossRef](#)]
30. Froula, D.H.; Glenzer, S.H.; Luhmann, N.C., Jr.; Sheffield, J. *Plasma Scattering of Electromagnetic Radiation: Theory and Measurement Techniques*; Elsevier Academic Press: Amsterdam, The Netherlands, 2011.
31. Gregori, G.; Schein, J.; Schwendinger, P.; Kortshagen, U.; Heberlein, J.; Pfender, E. Thomson scattering measurements in atmospheric plasma jets. *Phys. Rev. E* **1999**, *59*, 2286–2291. [[CrossRef](#)]
32. Narishige, S.; Kitamura, S.; Sakemi, S.; Tomita, K.; Uchino, K.; Muraoka, K.; Sakoda, T. Thomson scattering diagnostics of glow discharge plasmas produced in Raman active gases. *Jpn. J. Appl. Phys.* **2002**, *41*, 1259–1262. [[CrossRef](#)]
33. Palomares, J.M.; Hübner, S.; Carbone, E.A.D.; de Vries, N.; van Veldhuizen, E.M.; Sola, A.; Gamero, A.; van der Mullen, J.J.A.M. H_{β} Stark broadening in cold plasmas with low electron densities calibrated with Thomson scattering. *Spectrochim. Acta B* **2012**, *73*, 39–47. [[CrossRef](#)]
34. Carbone, E.A.D.; Nijdam, S. Thomson scattering on non-equilibrium low density plasmas: Principles, practice and challenges. *Plasma Phys. Control Fusion* **2015**, *57*, 014026. [[CrossRef](#)]
35. Continuum. Specification of Surelite I, II, III Series. 2002. Available online: https://amplitude-laser.com/wp-content/uploads/2019/03/Surelite-I-II-III_ref-d_BD.pdf (accessed on 13 March 2022).
36. Evans, D.E.; Katzenstein, J. Laser light scattering in laboratory plasmas. *Rep. Prog. Phys.* **1969**, *32*, 207–271. [[CrossRef](#)]
37. Jackson, J.D. *Classical Electrodynamics*, 3rd ed.; John Wiley & Sons Ltd.: Hoboken, NJ, USA, 1999.
38. Carbone, E.A.D.; Hübner, S.; Iordanova, E.; Palomares, J.M.; van der Mullen, J.J.A.M. Revision of the criterion to avoid electron heating during Laser Aided Plasma Diagnostics (LAPD). *J. Instrum.* **2012**, *7*, C01016. [[CrossRef](#)]
39. Palomares, J.M.; Iordanova, E.; Hübner, S.; Carbone, E.A.D.; van der Mullen, J.J.A.M. Towards poly-diagnostics on cool atmospheric plasmas. *J. Instrum.* **2012**, *7*, C02027. [[CrossRef](#)]
40. Forster, G. Bestimmung von Parametern Thermischer Plasmen Mittels Thomsonstreuung. Ph.D. Thesis, Bundeswehr University Munich, Neubiberg, Germany, 1995.
41. Compaan, A.; Wagoner, A.; Aydinli, A. Rotational Raman scattering in the instructional laboratory. *Am. J. Phys.* **1994**, *62*, 639–645. [[CrossRef](#)]
42. Miles, R.B.; Lempert, W.R.; Forkey, J.N. Laser Rayleigh scattering. *Meas. Sci. Technol.* **2001**, *12*, R33–R51. [[CrossRef](#)]
43. Kempkens, H.; Uhlenbusch, J. Scattering diagnostics of low-temperature plasmas (Rayleigh scattering, Thomson scattering, CARS). *Plasma Sources Sci. Technol.* **2000**, *9*, 492–506. [[CrossRef](#)]
44. Hoess, P. *4 Picos Ultra High Speed ICCD Camera Brochure*; Stanford Computer Optics Inc.: Berkeley, CA, USA, 2018.
45. Szulc, M.; Forster, G.; Marques, J.L.; Schein, J. Spectroscopic characterization of a pulsed low-current high-voltage discharge operated at atmospheric pressure. *Appl. Sci.* **2022**, *12*, 6366. [[CrossRef](#)]
46. Gao, L.; Feng, C.L.; Wang, Z.W.; Ding, H. High sensitive and high temporal and spatial resolved image of reactive species in atmospheric pressure surface discharge reactor by laser induced fluorescence. *Rev. Sci. Instrum.* **2017**, *88*, 053107. [[CrossRef](#)]
47. Nilson, D.G.; Hill, D.N.; Evans, J.C.; Carlstrom, T.N.; Hsieh, C.L.; Stockdale, R.E. Thomson scattering stray light reduction techniques using a CCD camera. *Rev. Sci. Instrum.* **1997**, *68*, 704–707. [[CrossRef](#)]
48. James, J.F. *Spectrograph Design Fundamentals*; Cambridge University Press: Cambridge, UK, 2007.
49. Sutton, J.A.; Driscoll, J.F. Rayleigh scattering cross sections of combustion species at 266, 355 and 532 nm for thermometry applications. *Opt. Lett.* **2004**, *29*, 2620–2622. [[CrossRef](#)] [[PubMed](#)]
50. Griem, H.R.; Lovberg, R.H. *Plasma Physics; Methods in Experimental Physics*; Academic Press Inc.: New York, NY, USA, 1970; Volume 9A.
51. Dowling, D.P.; O'Neill, F.T.; Langlais, S.J.; Law, V.J. Influence of a DC pulsed atmospheric pressure plasma jet processing conditions on polymer activation. *Plasma Process. Polym.* **2011**, *8*, 718–727. [[CrossRef](#)]
52. Kewitz, T.; Fröhlich, M.; von Frieling, J.; Kersten, H. Investigation of a commercial atmospheric pressure plasma jet by a newly designed calorimetric probe. *IEEE Trans. Plasma Sci.* **2015**, *43*, 1769–1773. [[CrossRef](#)]
53. Korzec, D.; Nettesheim, S. Application of a pulsed atmospheric arc plasma jet for low-density polyethylene coating. *Plasma Process. Polym.* **2020**, *17*, 1900098. [[CrossRef](#)]
54. Wiegand, C.; Beier, O.; Horn, K.; Pfuch, A.; Tölke, T.; Hipler, U.C.; Schimanski, A. Antimicrobial impact of cold atmospheric pressure plasma on medical critical yeasts and bacteria cultures. *Skin Pharmacol. Physiol.* **2014**, *27*, 25–35. [[CrossRef](#)]
55. Köhler, R.; Sauerbier, P.; Militz, H.; Viöl, W. Atmospheric pressure plasma coating of wood and MDF with polyester powder. *Coatings* **2017**, *7*, 171. [[CrossRef](#)]
56. Korzec, D.; Burger, D.; Nettesheim, S. Plasma activation from roll to roll. *Adhes. Adhes. Sealants* **2015**, *12*, 36–40. [[CrossRef](#)]

57. Szulc, M.; Schein, S.; Schaup, J.; Schein, J.; Zimmermann, S. Suitability of thermal plasmas for large-area bacteria inactivation on temperature-sensitive surfaces—First results with *Geobacillus stearothermophilus* spores. *J. Phys. Conf. Ser.* **2017**, *825*, 012017. [[CrossRef](#)]
58. Wallenhorst, L. Protective Particle Coatings Applied by Cold Plasma Spraying. Ph.D. Thesis, Georg-August University School of Science, Göttingen, Germany, 2017.
59. Reece Roth, J. *Industrial Plasma Engineering—Volume 1: Principles*; Institute of Physics Publishing: Bristol, UK, 1995.
60. Orrière, T.; Moreau, E.; Pai, D.Z. Ionization and recombination in nanosecond repetitively pulsed microplasmas in air at atmospheric pressure. *J. Phys. D Appl. Phys.* **2018**, *51*, 494002. [[CrossRef](#)]
61. Pai, D.Z.; Lacoste, D.A.; Laux, C.O. Nanosecond repetitively pulsed discharges in air at atmospheric pressure—The spark regime. *Plasma Sources Sci. Technol.* **2010**, *19*, 065015. [[CrossRef](#)]
62. Pai, D.Z.; Lacoste, D.A.; Laux, C.O. Transitions between corona, glow and spark regimes of nanosecond repetitively pulsed discharges in air at atmospheric pressure. *J. Appl. Phys.* **2010**, *107*, 093303. [[CrossRef](#)]
63. Lo, A.; Cessou, A.; Lacour, C.; Lecordier, B.; Boubert, P.; Xu, D.A.; Laux, C.O.; Vervisch, P. Streamer-to-spark transition initiated by a nanosecond overvoltage pulsed discharge in air. *Plasma Sources Sci. Technol.* **2017**, *26*, 045012. [[CrossRef](#)]
64. Gröger, S.; Ramakers, M.; Hamme, M.; Medrano, J.A.; Bibinov, N.; Gallucci, F.; Bogaerts, A.; Awakowicz, P. Characterization of a nitrogen gliding arc plasmatron using optical emission spectroscopy and high-speed camera. *J. Phys. D Appl. Phys.* **2018**, *52*, 065201. [[CrossRef](#)]
65. Becker, K.H.; Kogelschatz, U.; Schoenbach, K.H.; Barker, R.J. *Non-Equilibrium Air Plasmas at Atmospheric Pressure*; Plasma Physics; Institute of Physics Publishing: Bristol, UK, 2005.
66. Kong, C.; Gao, J.; Zhu, J.; Ehn, A.; Aldén, M.; Li, Z. Re-igniting the afterglow plasma column of an AC powered gliding arc discharge in atmospheric-pressure air. *Appl. Phys. Lett.* **2018**, *112*, 264101. [[CrossRef](#)]
67. Hontañón, E.; Palomares, J.M.; Stein, M.; Guo, X.; Engeln, R.; Nirschl, H.; Kruis, F.E. The transition from spark to arc discharge and its implications with respect to nanoparticle production. *J. Nanopart. Res.* **2013**, *15*, 1957. [[CrossRef](#)]
68. Kalra, C.S.; Cho, Y.I.; Gutsol, A.; Fridman, A.A.; Rufael, T.S. Gliding arc in tornado using a reverse vortex flow. *Rev. Sci. Instrum.* **2005**, *76*, 025110. [[CrossRef](#)]
69. Czernichowski, A.; Nassar, H.; Ranaivosoloarimanana, A.; Fridman, A.A.; Šimek, M.; Musiol, K.; Pawelec, E.; Dittrichova, L. Spectral and electrical diagnostics of gliding arc. *Acta Phys. Pol.* **1996**, *89*, 595–603. [[CrossRef](#)]
70. Gutsol, A.; Kossitsyn, M.; Fridman, A.A. Generation and diagnostics of non-equilibrium plasma in gliding arc discharge. In Proceedings of the Electronic proceedings of 16th International Symposium on Plasma Chemistry, Taormina, Italy, 22–27 June 2003.
71. Mutaf-Yardimci, O.; Saveliev, A.V.; Fridman, A.A.; Kennedy, L.A. Thermal and nonthermal regimes of gliding arc discharge in air flow. *J. Appl. Phys.* **2000**, *87*, 1632–1641. [[CrossRef](#)]
72. Machala, Z.; Laux, C.O.; Kruger, C.H.; Candler, G.V. Atmospheric air and nitrogen DC glow discharges with thermionic cathodes and swirl flow. In Proceedings of the 42nd AIAA Aerospace Sciences Meeting and Exhibit, Reno, NV, USA, 5–8 January 2004.
73. Lebouvier, A.; Delalandre, C.; Fresnet, F.; Boch, V.; Rohani, V.; Cauneau, F.; Fulcheri, L. Three-dimensional unsteady MHD modeling of a low-current high-voltage nontransferred DC plasma torch operating with air. *IEEE Trans. Plasma Sci.* **2011**, *39*, 1889–1899. [[CrossRef](#)]
74. Kubota, Y.; Ichiki, R.; Hara, T.; Yamaguchi, N.; Takemura, Y. Spectroscopic analysis of nitrogen atmospheric plasma jet. *J. Plasma Fusion Res.* **2009**, *8*, 740–743.
75. Kehler, M.; Duchoslav, J.; Hinterreiter, A.; Mehic, A.; Stehrer, T. Surface functionalization of polypropylene using a cold atmospheric pressure plasma jet with gas water mixtures. *Surf. Coat. Technol.* **2020**, *384*, 125170. [[CrossRef](#)]
76. Kewitz, T.; Regula, C.; Fröhlich, M.; Ihde, J.; Kersten, H. Influence of the nozzle head geometry on the energy flux of an atmospheric pressure plasma jet. *EPJ Tech. Instrum.* **2021**, *8*, 1. [[CrossRef](#)]
77. Pulpytel, J.; Kumar, V.; Peng, P.; Micheli, V.; Laidani, N.; Arefi-Khonsari, F. Deposition of organosilicon coatings by a non-equilibrium atmospheric pressure plasma jet: Design, analysis and macroscopic scaling law of the process. *Plasma Process. Polym.* **2011**, *8*, 664–675. [[CrossRef](#)]